Self-Activating Catalyst for Glucose Hydrogenation in the Aqueous Phase under Mild Conditions

A self-activating catalyst for glucose hydrogenation in aqueous phase under mild conditions

S. Esposito[1], B. Silvestri[2], V. Russo[3], B. Bonelli[4], M. Manzoli[5], F.A. Deorsola[4], A. Vergara[3], A. Aronne[2*], M. Di Serio[3,6*]

[1] Dipartimento di Ingegneria Civile e Meccanica e Unità INSTM, Università degli Studi di Cassino e del Lazio Meridionale, Via G. Di Blasio, 43, I-, Cassino (FR), 03043, Italy

[2]Dipartimento di Ingegneria Chimica, dei Materiali e della Produzione Industriale, Università di Napoli Federico II, P.le Tecchio, 80 I-80125 Napoli (Italy)

[3]Dipartimento di Scienze Chimiche, Università di Napoli Federico II, Via Cintia, 4 I-80126 Napoli

[4]Dipartimento di Scienza Applicata e tecnologia e Unità INSTM, Torino-Politecnico, Corso Duca degli Abruzzi, 24, I-, Torino, 10129, Italy

[5]Dipartimento di Scienza e Tecnologia del Farmaco, Università degli Studi di Torino, Via Pietro Giuria 9, 10125 Torino, Italy.

[6]International Research Organization for Advanced Science and Technology (IROAST), University of Kumamoto, 860-8555 Kumamoto, Japan.

Abstract

The search for efficient routs for the production of sorbitol from starch-derived glucose is of great interest and importance, as sorbitol is a highly attractive chemical for different application such as building block for the synthesis of fine chemicals, additives in food, cosmetic and paper industries. In this study a new nanomaterial, with the formula $(RuO_2)_{0.038}\cdot(SiO_2)_{0.962}$ was prepared by a one-pot sol-gel route. The performances of this new catalyst in the glucose hydrogenation reaction, in aqueous phase and mild conditions, are reported and compared with those of a commercial Ru/C catalyst. When commercial Ru/C was used as catalyst a high activity and no selectivity loss were observed, but the activity dramatically dropped already after the first cycles; on the contrary, the Ru-SiO_2 catalyst activity increased during the first three cycles. The different catalytic behavior was ascribed to the morphological distribution of Ru active phase in Ru-SiO_2 catalyst. Actually, the adopted synthesis procedure leads to a multimodal size distribution of the Ru nanoparticles, which are fairly stabilized by a combined interaction with the SiO_2 support and the reaction environment, which proved to be active in obtaining a self-activating catalyst.

Keywords: biomass valorization; self-activating catalyst; Ru-SiO_2; glucose hydrogenation, sorbitol; sol-gel synthesis.

1. Introduction

Biomass represents the main source for the production of renewable fuels and high-value industrial chemicals.[1] Sorbitol is one of most important value-added chemicals obtainable from lignocellulosic materials, thanks to the great variety of its applications such as building block for the synthesis of fine chemicals, additive in food, cosmetics and paper industries.[2] Actually, it can be used as substitute for food sweeteners, as intermediates in pharmaceutical production and as humectant in cosmetics. [2] Sorbitol is usually produced by chemical reduction of starch-derived glucose. It is obtained by catalytic hydrogenation of aqueous glucose solutions, either in discontinuous (autoclave) or continuous (tickle bed) reactors under high pressure (4-8 MPa) and in isothermal conditions at moderate temperature to avoid glucose degradation.[2] The reaction occurs directly between glucose and molecular hydrogen in the presence of a catalyst and there are several pathways that can occur leading to the formation of by-products, as shown in Scheme 1.

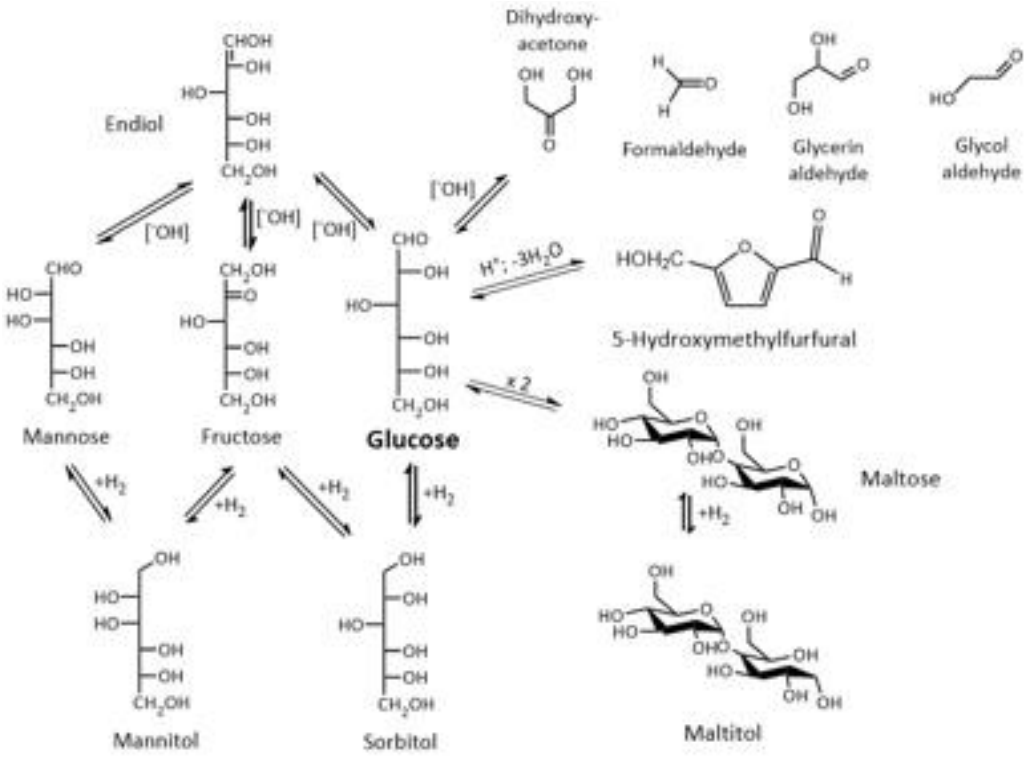

Scheme 1. Reaction network for hydrogenation of glucose.

By non-catalytic pathways, mannose and fructose can be obtained as products of the Lobry de Bruyn–Alberda van Ekenstein rearrangement. Glycerin aldehyde, dihydroxyacetone, glycol aldehyde and formaldehyde can form in alkaline conditions, whereas 5-hydroxymethylfurfural can be obtained by dehydration.[2] Maltose is the product of

dimerization of glucose. Therefore, mannitol, which is the product of the hydrogenation of fructose and mannose, may be the main by-product of the reaction even if yields higher than 90% in sorbitol can be obtained.[2]

The used heterogeneous catalysts are transition metals supported on porous matrices, such as oxides and carbons. Nickel is widely used, even if leaching problems, leading to a reduction of the catalytic activity as well as a difficult product purification, are the main drawbacks.[3] Furthermore, for food, medical and cosmetic applications, nickel must be completely removed from the products, resulting in high additional costs, being 2 mg kg^{-1} the maximum permitted Ni concentration in food industry.[4]

Among noble metals, ruthenium seems to show the best catalytic performances, 50 times higher in comparison with nickel, avoiding leaching.[5,6] Therefore, to obtain similar performance, a lower amount of ruthenium is required allowing the compensation of its higher cost. Moreover Ru-based catalysts exhibit also lower downtime, due to the prolonged lifetime of the catalyst.[2] Besides the metal content, the catalytic performances of Ru-based catalysts are mainly influenced by the support. In recent years, several inert solids were proposed as suitable support in which ruthenium nanoparticles were homogenously dispersed. Even if some interesting results, summarized in Table 1, were obtained, a stable anchoring of the metal onto the support seems to be still not achieved.

According to the literature, carbon supported Ru catalysts displayed higher activity than the Raney nickel ones and did not leach in reaction conditions.[5,7] However, these catalysts showed high deactivation in operation conditions.[8]

Catalysts based on Ru dispersed on SiO_2 (Ru/SiO_2) and TiO_2 (Ru/TiO_2) showed higher conversion for Ru/SiO_2 (98.5%) than Ru/TiO_2 (56.8%),[9] the difference having been related to the different surface area of the supports. Notwithstanding the high activity, subsequent deactivation was rapid, due to the deposition of oligomeric species at the catalyst surface. Ru/Al_2O_3 catalysts, in continuous hydrogenation of glucose, showed high deactivation due to the formation of gluconic acid, acting as poisoning agent.[10] Ru/MCM-41 silica catalyst showed higher catalytic activity than carbon supported Ru catalysts, but after the first reuse the sorbitol yield decreased from 83.13 down 68.21%[11]: though the catalyst did not show significant leaching after several recycle times, after the fourth recycle a remarkable agglomeration of Ru particles was observed. Recently, a bimetallic Ru:Ni/MCM-48 catalyst was proposed for glucose hydrogenation,[12] and the influence of different Ru content was tested, showing an optimum ratio of Ru:Ni = 0.45. The catalyst showed good stability after three reaction cycles (270 min). Innovative supports formed by $NiO\text{-}TiO_2$ mixed oxides were

proposed for the glucose hydrogenation in liquid phase, obtaining total conversion and high selectivity, but a metal leaching was still observed.[13,14] Zeolites were also proposed as matrix for Ru immobilization (i.e. Ru(1.0%)/HYZ), showing high sorbitol selectivity (up to 98.7%), with small amount of mannitol as by-product,[15] but only in more severe reaction conditions (140 °C and 5.5 MPa).[16]

Table 1 - Comparison of different Ru-based catalysts.

Catalysts	Substrate	Ru [%wt]	*p* [MPa]	*T* [°C]	*t* [min]	$X_{substrate}$ *%conversion*	$\Phi_{sorbitol}$ *%selectivity*
C supported Ru [5,7]	Glucose	3.5-5.0	1.0-6.0	100-140	140-200	100	>98
Ru/TiO_2 [9]	HPA	1.0-1.2	0.55	190	360	56.8	n.d.
Ru/SiO_2 [9]	HPA	3.7	0.55	190	360	98.5	n.d.
Ru/MCM-41 [11,12]	Glucose	5	3	120	180	~100	83.1
Ru/NiO_TiO_2 [13,14]	Glucose	1	2.5	120-140	90	94.9	97.2
Ru/HYZ [15]	Glucose	1	2-5.5	100-140	180	~100	>98.7

As revealed by the literature survey, the stability of the catalyst mainly depends on the kind of interaction between the matrix and the metal that, in turn, derives from the adopted immobilization and synthesis procedure.

Among those, the sol–gel process with its mild conditions and tunable synthesis parameters provides huge opportunities to produce hybrid organic–inorganic mesostrucutured materials with intimate mixing and tailored interface between the matrix and the active species.[17-20]

In this context, we recently proved that Ru nanoparticles (*ca.* 3.0 nm in size) can be efficiently immobilized in a Nb_2O_5-SiO_2 matrix by an innovative sol-gel synthesis, giving an active and stable catalyst for the levulinic acid hydrogenation to γ-valerolactone.[21] Following this strategy, in this work a new $(RuO_2)_{0.038}\cdot(SiO_2)_{0.962}$ nanomaterial was prepared, which proved to be a self-activating catalyst for glucose hydrogenation. Here, a matrix with a lower acid character than the Nb_2O_5-SiO_2 mixed oxides was selected, with the aim to limit the (undesired) glucose isomerization. In the present work, the performances of Ru-SiO_2 catalyst in the glucose hydrogenation reaction, in aqueous phase and mild conditions, are reported and compared with those of a commercial Ru/C catalyst. Particularly, the self-activating ability of the new catalyst is discussed in respect of its physico-chemical properties.

2. Materials and methods

2.1 Reagents

The following reagents by Sigma-Aldrich were used: tetraethoxysilane (TEOS, $Si(OC_2H_5)_4$ 99%), anhydrous ethanol (EtOH), ruthenium (III) chloride-3-hydrate ($RuCl_3 \cdot 3H_2O$ 99.98%), D-glucose ($C_6H_{12}O_6$, ≥ 99.5%), D-sorbitol ($C_6H_{14}O_6$, ≥ 98%). Commercial catalyst 5.0 wt% Ru/C was purchased by TCI.

2.2 Sol-gel synthesis

The composition of the synthesized material can be expressed by the following formula: $(RuO_2)_{0.038}$ $(SiO_2)_{0.962,}$ which corresponds to a metallic ruthenium content of 6.30 wt % after complete reduction.

A hydro-alcoholic solution of TEOS (18.6 mL), having a molar ratio TEOS : EtOH : H_2O = 1: 4 : 4 was prepared at room temperature. A proper amount of $RuCl_3 \cdot 3H_2O$ (870 mg) was added and the solution was stirred until a reddish solution was obtained. Finally, some drops of HCl hydro-alcoholic solution were slowly added to obtain a final molar ratio TEOS:HCl = 1:0.073. From this final solution, a transparent dark-red gel was obtained within 18 days. The gel was kept 3 days at room temperature before drying, and afterwards it was fully dried in air at 110 °C in an electric oven until a constant weight was reached. After such treatments, amorphous hardened dry gels were obtained. Finally, samples were annealed for 2 h at 500 °C in air.

2.3 Catalytic tests

The tested catalysts were pre-reduced at 300 °C and 0.1 MPa for 3 h, in a dedicated packed-bed reactor under a 0.1 L min^{-1} H_2 flow (Scheme 2A). The reduced catalyst was cooled at room temperature under H_2 flow and then quickly charged to the vessel. Glucose hydrogenation to sorbitol was performed in a fed-batch reactor (Scheme 2B), where H_2 was fed at constant pressure (roughly 2.0 MPa) to a 0.3 L vessel charged with 200 g of a glucose liquid solution at 0.1 mol L^{-1} concentration. The reaction mixture, containing the catalyst (*ca.* 0.5 g), was flushed with N_2 at 0.5 MPa, to evacuate the dissolved O_2 before H_2 feeding. Temperature was increased at the desired value (120 °C), and the solution was stirred at 600 rpm. After about 10 washes, H_2 was fed to the reactor at the desired pressure and the reaction started. Samples were periodically withdrawn from the reaction vessel, to evaluate the evolution with time of both glucose conversion and sorbitol selectivity. An AISI 316 stainless steel net was installed at the bottom of the withdrawn pipe to avoid any catalyst loss. For each

catalyst, the reuse experiments were made by performing cycles of 5 experiments. Once a single experiment ended, the catalyst was washed with distilled water and reused after filtration for a new experimental test performed in the same operating conditions. Temperature and H_2 flow were measured by means of a National Instruments DAQ device, equipped with a homemade acquisition software written in LabView 2013. The collected sample composition was analyzed via HPLC, by using a Rezex Monosaccharide Ca^{2+}, by using $1.2 \cdot 10^{-3}$ mol L^{-1} $CaSO_4$ aqueous solution, fixing the column temperature at 85 °C, liquid flow-rate at 0.7 mL min^{-1} and loading 1 µL of the collected sample. The species were analyzed via RI detector. Retention times were detected as it follows: glucose 9 min, mannitol 17 min, sorbitol 21 min. Calibration curves were built for each component by using dedicated standards.

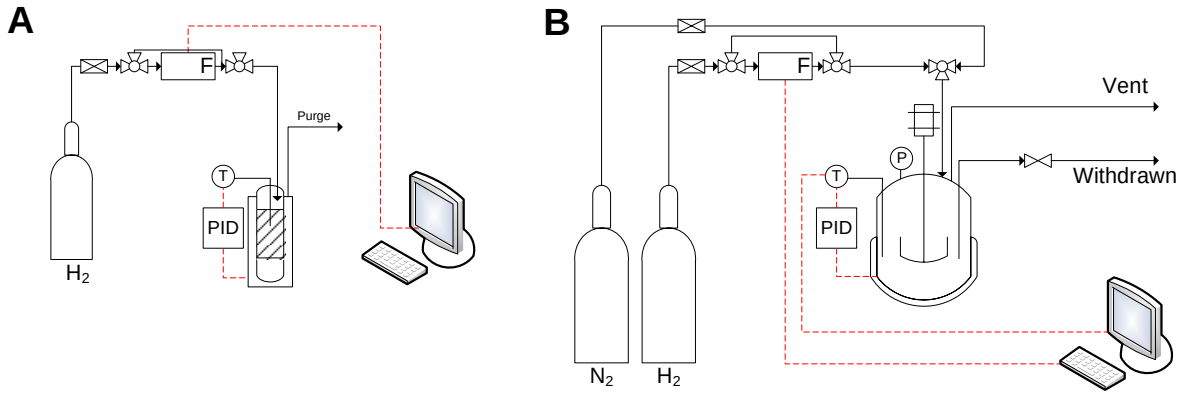

Scheme 2 – Experimental setup for: A. catalyst reduction; B. hydrogenation tests.

2.4 Catalyst characterization

2.4.1 TPR (Temperature Programmed Reduction) analysis

TPR measurements (Figure S1) were carried out on a TPD/R/O 1100 instrument (ThermoQuest) equipped with thermal conductivity detector (TCD) by using a 5 vol.% H_2/Ar mixture (Q = 20 cm^3 min^{-1}) with a heating rate of 10 °C min^{-1} up to 800 °C. In a typical experiment, ca. 100 mg sample was loaded in a quartz down-flow cell with a K thermocouple placed in close contact with the sample to measure the temperature. On the same instrument, CO-pulse chemisorption experiments were carried out. The pretreatment procedure was performed as follows: ca. 150 mg of sample was placed in the quartz reactor and heated under a N_2 flow of 20 cm^3 min^{-1} up to 300 °C (heating rate 10 °C min^{-1}, soak time 30 min). Subsequently, the sample was reduced under a H_2 flow of 60 cm^3 min^{-1} at 300 °C for 3 h, then cleaned under a flow of N_2 (Q = 20 cm^3 min^{-1}) at the same temperature and finally cooled

down at room temperature. Chemisorption measurements were performed by pulsing each time 0,791 cm^3 of a 10 vol% CO/He mixture until surface saturation. The measured amount of chemisorbed CO was employed for determining the ruthenium dispersion, assuming a molar stoichiometric factor CO/Ru=1.

2.4.2 High Resolution Transmission Microscopy

Transmission electron microscopy (TEM) and High Resolution (HR-) TEM micrographs were obtained using a JEOL 3010-UHR instrument operating at 300 kV, equipped with a LaB_6 filament and fitted with X-ray EDS analysis by a Link ISIS 200 detector. Digital micrographs were acquired by a 2k × 2k pixel Gatan US1000 CCD camera. The samples in the form of powders were deposited on a copper grid covered with a lacey carbon film. Histograms of the Ru particle size distribution were obtained by considering a statistical representative number of particles (from > 600 up to > 700 for each examined sample) on the HR-TEM images, and the mean particle diameter (d_m) was calculated as:

$$d_m = \Sigma d_i n_i / \Sigma n_i \quad (1)$$

where n_i was the number of particles of diameter d_i.

Furthermore, the Ru Specific Surface Area (Ru SSA, m^2/g) of the supported metal particles (supposed to be spherical) was calculated basing on the corresponding particle size distribution, by applying Eq. (2):

$$\text{Ru SSA} = 3\Sigma n_i r_i^2 / (\rho_{Ru} \Sigma n_i r_i^3) \quad (2)$$

where r_i is the mean radius of the size class containing n_i particles, and ρ_{Ru} the volumetric mass of Ru (12.41 g/cm^3). The amount of catalyst used in the catalytic tests (*ca.* 0.5 g) and the Ru loading of the Ru/C and Ru-SiO_2 catalysts (5.0 and 6.30 wt%, respectively) were considered to evaluate the theoretical metal area (Ru SA, m^2)

2.4.3 N_2 adsorption/desorption isotherms at -196 °C

N_2 isotherms were measured at -196 °C on ca. 100 mg powder previously outgassed at 300 °C for 3 h in order to remove water and other atmospheric contaminants (Quantachrome Autosorb 1 instrument). Specific Surface Area (SSA) values of the powder was calculated according to the BET (Brunauer-Emmett-Teller) method.

2.4.4 XP Spectroscopy (XPS)

X-ray photoelectron spectroscopy (XPS) analysis was carried out on XPS PHI 5000 Versa probe apparatus, using a band-pass energy of 187.85 eV, a 45 ° take off angle and a 100.0 μm

diameter X-ray spot size for survey spectra. High-resolution XP spectra were recorded in the following conditions: pass energy of 20 eV, resolution of 1.1 eV, and step of 0.2 eV. Sample charging effects were eliminated by referring to the spectral line shift to the C 1s binding energy (BE) value of 284.8 eV. XP-spectra were analysed by means of a commercial software (CasaXPS, version 2.3.16), by applying mixed Gaussian-Lorentzian (70-30 %) profiles.

*2.4.*5 *Raman Microspectroscopy*

A confocal Raman microscope (Jasco, NRS- 3100) was used to collect Raman spectra. The 514 nm line of a water cooled Ar^+ laser, 4 mW at the sample, was injected into an integrated Olympus microscope and focused to a spot diameter of approximately 2 μm by a 100× objective. A holographic notch filter was used to reject the excitation laser line. Raman scattering was collected by a Peltier-cooled 1024×128 pixel CCD photon detector (Andor DU401BVI). Raman measurements were at least triplicated for scope of reproducibility. Cyclohexane was used for calibration.

3 Results and discussion

3.1. TPR analysis and catalytic tests

The TPR analysis carried out on the as-purchased commercial Ru/C powder (Figure S1) showed two main reduction peaks at 240 °C, assigned to one-step reduction of Ru^{4+} species to Ru^0 [22] and at 335 °C, assigned to partial gasification of the support with consequent H_2 consumption due to the formation of CH_4.[22,23] As the TPR results indicated the occurrence of some (oxidized) Ru^{4+} species in the as-purchased catalyst, the powder was pre-reduced at 300 °C, a temperature (T) both ensuring Ru reduction and avoiding the support gasification. The commercial catalyst was indeed tested both as purchased and pre-reduced at 300 °C (Ru/C): the collected data, however, did not differ much before (Figure S2) and after reduction at 300 °C (Figure 1A), indicating a similar degree of Ru reduction in the two powders. Such finding, apparently in contrast with the presence of Ru^{4+} revealed by TPR analysis, could be ascribed either to some heterogeneity in the commercial powder or to a partial surface oxidation of Ru particles due to evaporation of the protective solvent, in agreement with XPS analysis (*vide infra*).

The $(RuO_2)_{0.038}\cdot(SiO_2)_{0.962}$ sample was pre-reduced at 300 °C (Ru-SiO_2), as TPR analysis (Figure S3) showed a minor peak at low T (130 °C), ascribed to the thermal decomposition/reduction of the ruthenium precursor ($RuCl_3\cdot 3H_2O$), along with two main reduction peaks at *ca.* 230 and 290 °C. The peaks were ascribed to the occurrence of two

types of RuO_2 species with different reducibility, in that the low T H_2 consumption could be due to the occurrence of a highly dispersed RuO_2 phase, weakly interacting with the support, and the high T peak to the occurrence of larger and less dispersed RuO_2 particles, likely the crystalline RuO_2 phase detected by Raman spectroscopy (*vide infra*). With the same catalyst, a further H_2 consumption was measured above 500 °C, likely due to some H_2 spillover phenomenon occurring on the formed Ru^0 particles.[24,25]

Catalytic tests were performed by re-using the catalysts and measuring the glucose conversion ($X_{glucose}$, full symbols, Figure 1) and sorbitol selectivity ($\Phi_{sorbitol}$, empty symbols, Figure 1) trends during time. Figure 1A shows the re-usability tests of Ru/C for 5 cycles of 60 min each, while Figure 1B the performance of Ru-SiO_2 for 5 cycles of 300 min each, the duration of each cycle being determined by the different activities of the catalysts.

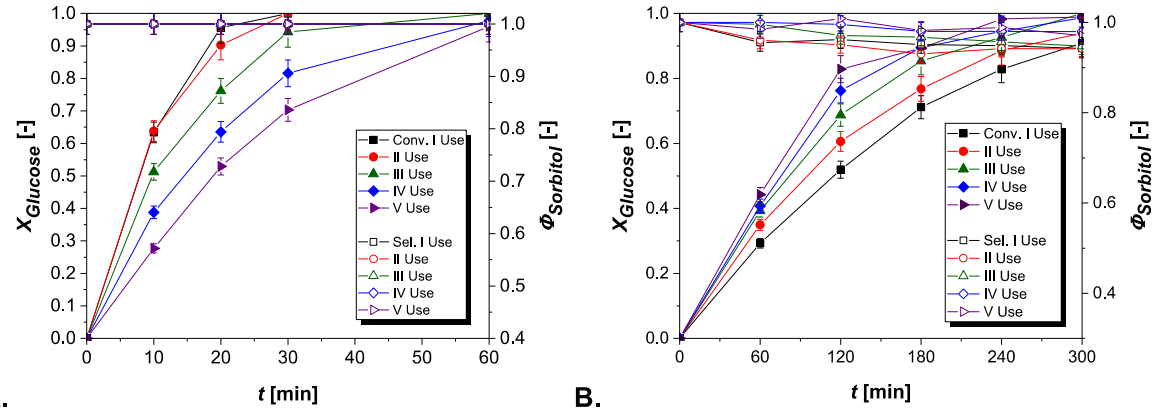

Figure 1. Glucose conversion ($X_{glucose}$) and sorbitol selectivity ($\Phi_{sorbitol}$) trend for each re-use cycle performed using: A. Ru/C; B. Ru-SiO_2. Reaction conditions: p = 2.0 MPa, $c_{Glucose}(t=0)$ = 0.1 mol/L, catalyst loading = 0.5 g, T = 120°C, stirring rate = 600 rpm.

Interestingly, the Ru/C catalyst shows high activity and no selectivity loss (Figure 1A), but its activity dramatically drops already after the first two cycles, though keeping total selectivity to sorbitol (Figure 1A). On the contrary, the Ru-SiO_2 catalyst activity increases during the first three cycles and then it remains almost constant (Figure 1B). The same occurs for the selectivity to sorbitol, mannitol being the unique detected by-product of the reaction in the adopted operation conditions.

The TOF (turn-over-frequency) was computed in agreement with Eq. 3 to calculate the activity of each catalyst, the results being reported in Figure 2A-B.

$$TOF = \frac{1}{n_{Ru}} \frac{dn_{glucose}}{dt} \qquad (3)$$

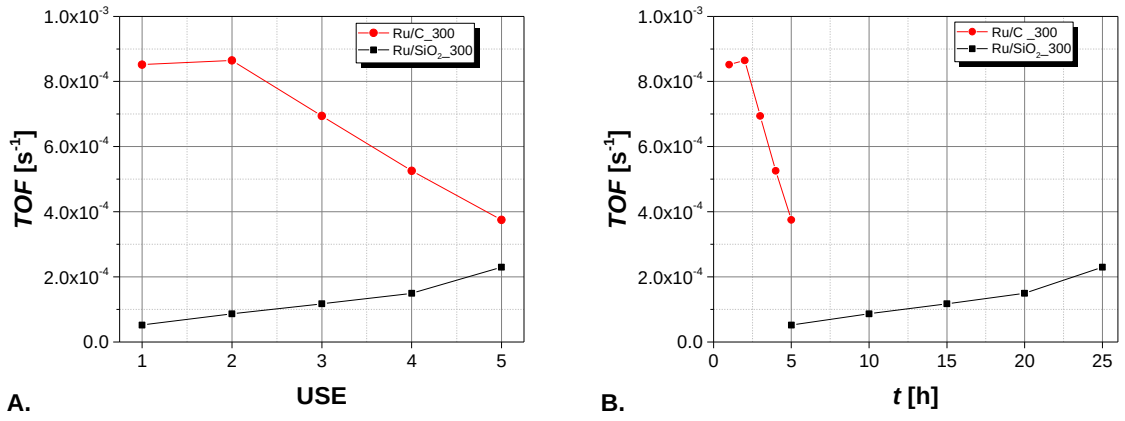

Figure 2. TOF trend for the catalysts as a function of: A. re-use cycles; B. cumulative time.

As shown in Figure 2A, Ru/C shows the highest activity during the first cycle, then the activity drops very rapidly, demonstrating a fast deactivation of the catalyst. Conversely, the Ru-SiO_2 TOF values increased with time, reaching roughly the same activity showed by Ru/C after 5 cycles. It must be reminded that each Ru-SiO_2 cycle lasts 5 h, whereas each Ru/C cycle only lasts 1 h, therefore the TOF values clearly mean that Ru/C activity is already lost in 5 h, whereas Ru-SiO_2 is getting activated in the first 5 h. This fact is even more evident in Figure 2B, where the TOF values are plotted against the cumulative time: Ru/C is very active, but it loses its activity in a short time, while Ru-SiO_2 shows a self-activating behavior as the reaction proceeds.

To verify the reduction of the sample in the reaction environment, two experiments were run with the $(RuO_2)_{0.038}\cdot(SiO_2)_{0.962}$ sample, *i.e.* without the pre-reduction step, using it for two catalytic cycles. The results are displayed in Figure 3.

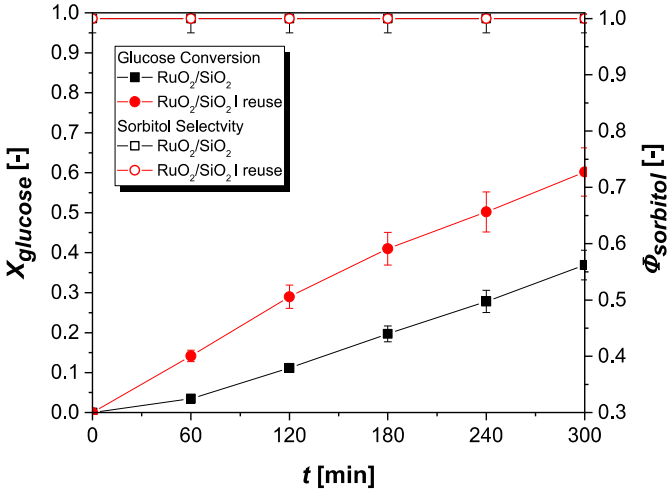

Figure 3. Glucose conversion ($X_{glucose}$) and sorbitol selectivity ($\Phi_{sorbitol}$) trend for each re-use cycle by using the $(RuO_2)_{0.038}\cdot(SiO_2)_{0.962}$ sample (not pre-reduced). Reaction conditions: p = 2.0 MPa, $c_{Glucose}(t = 0)$ = 0.1 mol/L, catalyst loading = 0.5 g, T = 120°C, stirring rate = 600 rpm.

Interestingly, $(RuO_2)_{0.038}\cdot(SiO_2)_{0.962}$ sample gets activated as the reaction proceeds, thus both H_2 and glucose in liquid phase are able to slowly reduce it, synergistically. Thus, $(RuO_2)_{0.038}\cdot(SiO_2)_{0.962}$ is reduced at low temperature in the same hydrogenation reactor, without pre-reducing treatment. Two experiments were performed by trying to separate the effect of H_2 and glucose on the catalyst activation. The former experiment was conducted by putting the $(RuO_2)_{0.038}\cdot(SiO_2)_{0.962}$ catalyst in water under H_2 pressure for 25 h at 120 °C, then glucose was added, and the reaction started. Only a small glucose conversion was obtained in 5 h of reaction ($X_{glucose}$=3%). The latter experiment was performed by placing in contact the $(RuO_2)_{0.038}\cdot(SiO_2)_{0.962}$ sample with an aqueous solution of glucose for 25 h at 120 °C. Then, H_2 was added, and the reaction started. A negligible conversion was obtained also in this case ($X_{glucose}$=5%). These experiments clearly demonstrate that only the synergic effect of both H_2 and glucose is able to slightly reduce the catalyst *in situ*, provided that the catalyst has been pre-reduced.

3.2.Physico-chemical characterization of the catalysts

TEM measurements were carried out on the Ru/C catalyst after 5 cycles (referred to as Ru/C_5c), with the aim of investigating the decrease of activity. The results are shown in Figure 4 and Figure S4. A representative TEM image of the Ru/C along with the Ru particle size distribution are shown in Figure 4A and B, respectively. Very small Ru nanoparticles, homogeneously distributed on amorphous carbon (see Figure S4, A. and B. panels), with spherical shape and regular size are observed. Most of them have a diameter between 2 and 3 nm, and average particle size of 2.4 ± 0.5 nm. The diffraction fringes related to the presence of the (101) plane of metallic Ru in the hexagonal phase (JCPDS file number 00-001-1253) were also observed on the Ru/C catalyst by HR-TEM analysis (panel A. of Figure S4).

A broadening of the particle size distribution, resulting from the Ru nanoparticle agglomeration during reaction, occurs after 5 catalytic runs (panel D. of Figure 4), leading to a mean diameter of the nanoparticles equal to 3.0 ± 0.8 nm (see also Table 2). Moreover, no diffraction fringes due to crystalline Ru^0 were detected by HR-TEM on the Ru/C_5c catalyst.

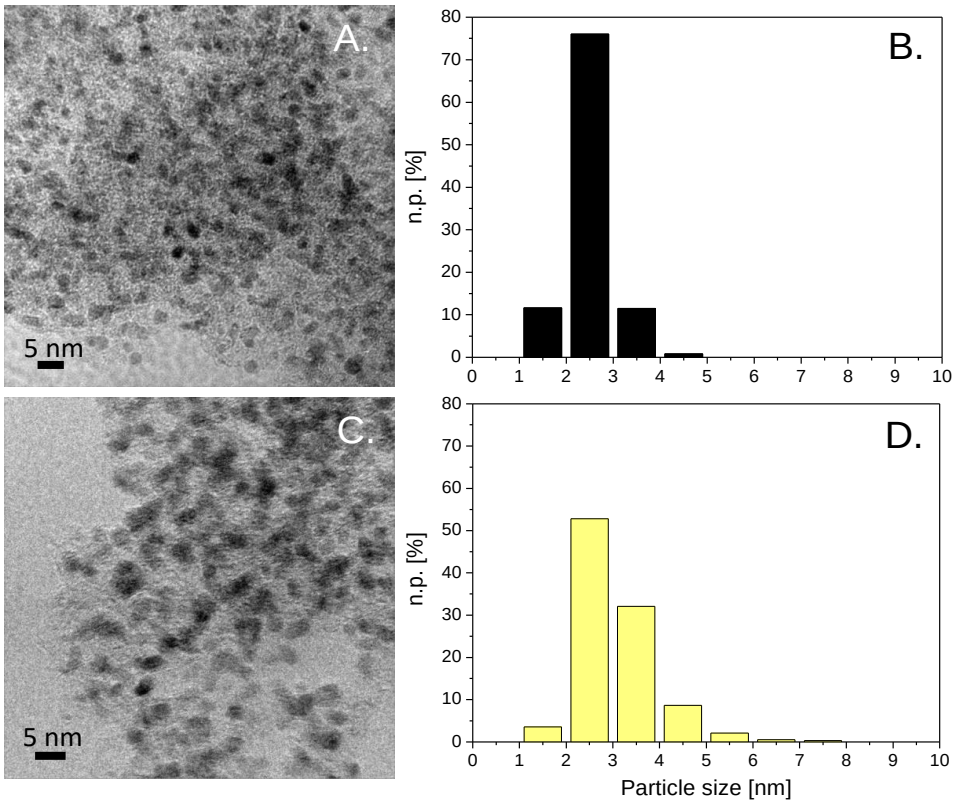

Figure 4. TEM images and Ru particle size distributions of: A. and B. Ru/C catalyst; C. and D. Ru/C_5c catalyst. Instrumental magnification: A. 250000X; B. 300000X.

Basing on the particle size distributions, the corresponding Ru SSA (m^2/g) of the supported metal nanoparticles (supposed to be spherical) was calculated. In addition, the theoretical metal area (Ru SA, m^2) was also evaluated, by considering the amount of catalyst used in the catalytic tests and the Ru loading. The results are summarised in Table 2.

Table 2. Ru average size, metal SSA and SA by TEM analysis for the Ru/C and Ru-SiO_2 catalysts. Catalysts BET SSA by N_2 adsorption/desorption isotherms at -196 °C.

Catalyst	**Ru average size (nm)**	**Ru SSA (m^2/g)**	**Ru SA (m^2)[a]**	**BET SSA ($m^2\ g^{-1}$)**
Ru/C	2.4 ± 0.5	88.7	2.2	840
Ru/C_5c	3.0 ± 0.8	67.4	1.7	840
Ru-SiO_2	2.9 ± 0.1	57.8	1.8	523
Ru-SiO_2_5c	3.7 ± 0.1	52.8	1.7	577

[a] Calculated basing on the amount of catalyst used (*ca.* 0.5 g) and the Ru loading: 5.0 wt% (Ru/C) and 6.30 wt% (Ru-SiO_2).

Particularly, it was found that the Ru/C catalyst exposes a metal SSA equal to 88.7 m^2/g, which decreases to 67.4 m^2/g after 5 cycles. These features correspond to a drop of the theoretical Ru SA from 2.2 to 1.7 m^2 and agree with the fast deactivation of the Ru/C catalyst, also by considering that the BET SSA (Table 2) remains practically unchanged after 5 cycles, indicating that the deactivation is mostly due to changes related to Ru nanoparticles, not efficiently stabilized by the C support.

Large Ru particle agglomerates were observed at low magnification on the Ru-SiO_2 catalyst (the images have been taken on several different regions of the grid), as shown in panel A. of Figure S5. On these agglomerates, the spacing related to the (100) and (101) planes of hexagonal Ru (JCPDS file number 00-001-1253) were found. However, at higher magnification, the TEM images of the Ru-SiO_2 catalyst showed a large amount of small (Figure 5, panel A.) and very small (panel B., highlighted by dashed orange circles) Ru nanoparticles, indicating that on this catalyst the size of the Ru active phase is heterogeneous. The Ru particle size distribution is reported in panel C of the same figure.

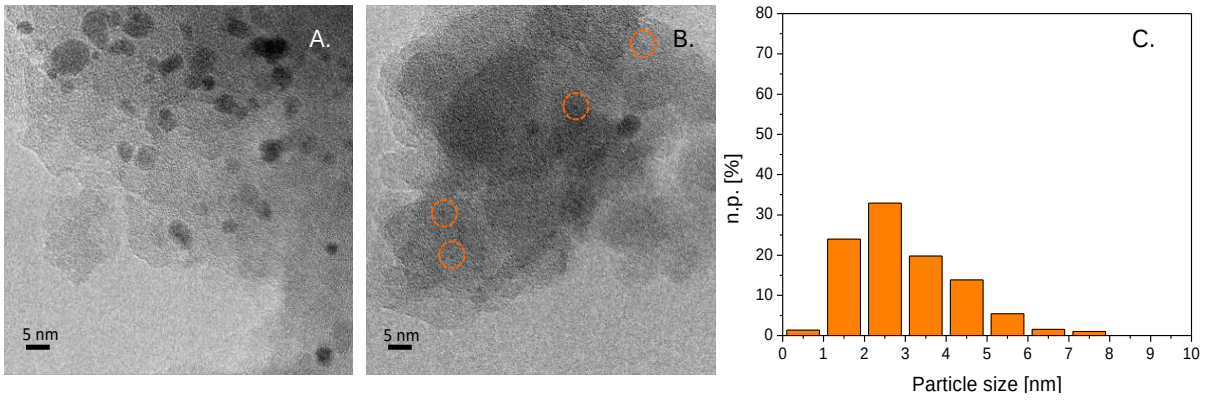

Figure 5. TEM images of Ru-SiO_2: A. and B. (in which the very small Ru nanoparticles are highlighted by dashed orange circles) panels and Ru particle size distribution C. panel. Instrumental magnification: 250000X.

With Ru-SiO_2, Ru nanoparticles have globular shape and mean diameter of 2.9 ± 0.1 nm (about 600 nanoparticles were counted). Only these Ru nanoparticles were considered to calculate the Ru SSA, as the large Ru agglomerates poorly contribute to this parameter and, reasonably, to the catalytic activity. A Ru SSA equal to 57.8 m^2/g was found for the Ru-SiO_2 catalyst (Table 2). With the Ru-SiO_2_5c (*i.e.* after 25 h reaction), along with Ru agglomerates (panel B of Figure S5), nanoparticles (panel A of Figure 6) with average size of 3.7 ± 0.1 nm (> 700 particles were counted to build the distribution) were also observed. In addition, the

particle size distribution is quite similar to the Ru-SiO_2 catalyst and the Ru SSA slightly decreases to 52.8 m^2/g. In contrast with what observed with the Ru/C_5c catalyst, the Ru SSA does not vary much after the five cycles, indicating that the Ru nanoparticles are fairly stabilized by the interaction with the SiO_2 support, likely because of the adopted synthesis procedure. Indeed, the theoretical Ru SA is essentially unchanged after 25 h reaction (from 1.8 to 1.7 m^2) as shown in Table 2. The corresponding increase in the BET SSA (Table 2) of Ru-SiO_2_5c is likely ascribed to changes in the silica structure occurring in aqueous phase, as revealed by Raman spectra discussed below.

Interestingly, zones (as that put in evidence in panel A of Figure 6) in which diffraction fringes with spacing typical of the (101) plane of hexagonal Ru (JCPDS file number 00-001-1253) were observed. This feature could be due to the presence of highly dispersed Ru^{4+} species on the $(RuO_2)_{0.038}\cdot(SiO_2)_{0.962}$ sample, that are gradually reduced to Ru upon reduction at 300 °C and after 25 h of reaction resulting in the formation of thin crystalline layers of metallic ruthenium. This finding is in fair agreement with literature data showing that Ru^{4+} species are easily reducible when supported on SiO_2. [26]

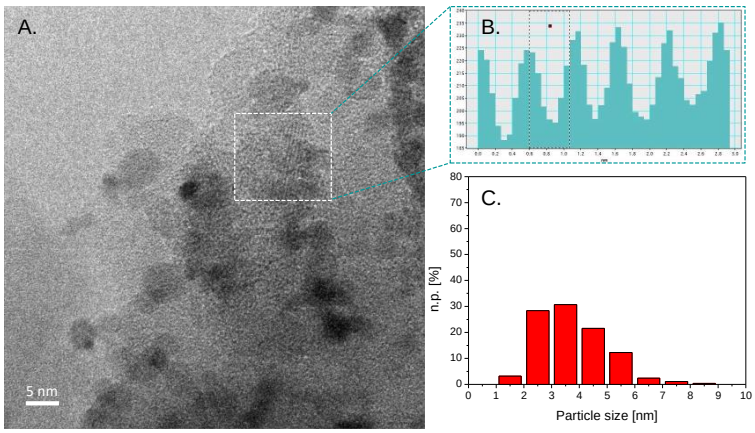

Figure 6. A. HR-TEM image of Ru-SiO_2_5c catalyst, B. measure of the spacing between the diffraction fringes observed in the zone highlighted by the white dashed square and C Ru particle size distribution. Instrumental magnification: 300000X.

In agreement with TPR analysis (*vide supra*), with the as purchased Ru/C sample (spectra not shown) only Ru^{4+} species were detected by XPS analysis: this result, apparently in contrast with the catalytic activity of the fresh catalyst (Figure S2), is indeed in agreement with the fact that the powder was exposed to air to induce spontaneous evaporation of the protective solvent before XPS measurements, with a consequent oxidation on the surface of Ru particles. Correspondingly, in the O 1s region two components were found, assigned to C-O (532.4 eV)

and O=C-O (530.8 eV) groups,[27] the latter likely coordinating surface Ru^{4+} species. Figure 7 reports the curve-fitting of the XP spectra performed on the Ru(3d)5/2 and the O(1s) core levels of the Ru/C (pre and Ru/C_5c catalysts. The curve-fitting of Ru(3d)5/2 line with the Ru/C catalyst showed the occurrence of two components, respectively assigned to (unreduced) Ru^{4+} species and to reduced ruthenium (*ca* 32.6 %). The latter line was observed at 280.5 eV, *i.e.* a slightly higher binding energy value with respect to literature values reported for Ru^{0} species. In the O 1s region, the curve-fitting procedure led to the identification of two main components at 531.0 and 532.7 eV, assigned to O=C-O and C-O groups respectively. The limited reduction of surface Ru species is likely due to surface C-containing groups acting as ligands and stabilizing the Ru^{4+} species, in agreement with the fact that the catalyst activity does not differ much from that of the fresh powder, because reduction affects only a fraction of the actually present ruthenium. With the Ru/C_5c catalyst, the overall amount of Ru^{4+} species increased (Table 3), in agreement with its deactivation observed during the catalytic tests. The progressive catalyst oxidation was confirmed by the inspection of the O 1s region, where two components were identified at 530.4 and 532.1 eV corresponding to C=O and O=C-O bonds respectively, whereas the component due to (formerly present) C-O species was not observed.

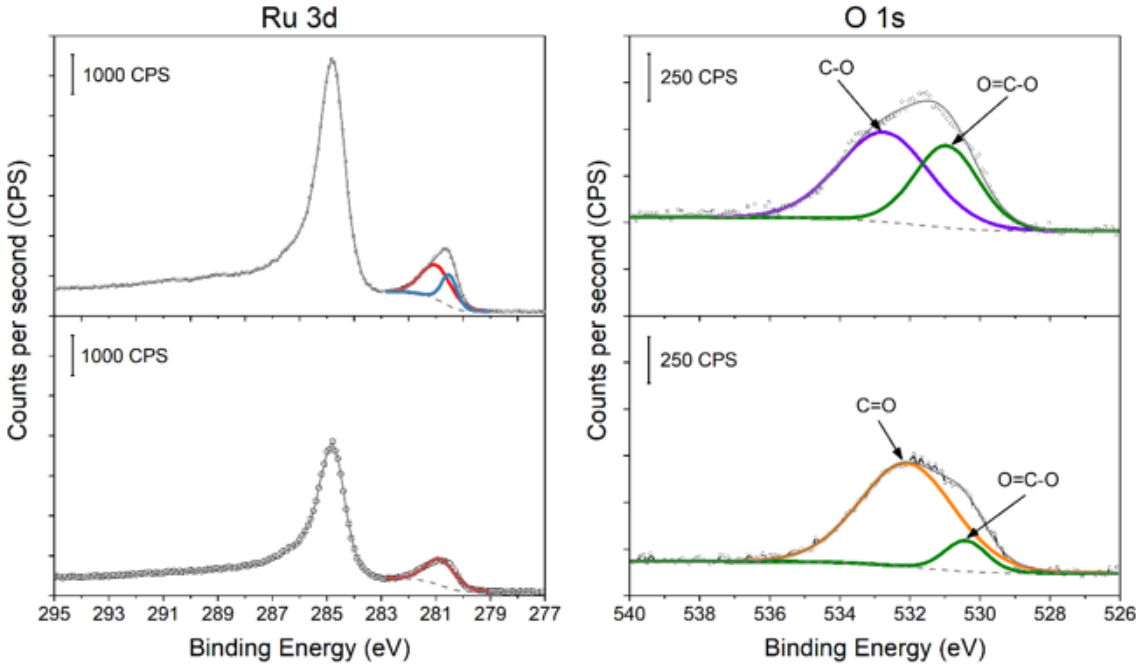

Figure 7. Ru(3d)5/2 and the O(1s) core levels XP spectra of the Ru/C (top panel) and Ru/C_5c catalysts (bottom panel).

Table 3. Values of binding energy (BE, eV) and surface relative concentration (SRC, %) as obtained by the curve-fitting procedure carried out on the XP analyses of Ru/C as purchased, Ru/C and Ru/C_5c catalysts.

Sample			Ru/C as purchased	Ru/C	Ru/C_5c
O 1s	O=C-O	BE [eV]	530.8	531.0	530.4
		% SRC	34.9	33.5	11.8
	C=O	BE [eV]	-	-	532.1
		% SRC	-	-	88.2
	C-O	BE [eV]	532.4	532.7	-
		% SRC	65.1	60.7	-
Ru $3d_{5/2}$	Ru	BE [eV]	-	280.5	-
		% SRC	-	32.6	-
	Ru^{4+}	BE [eV]	281.4	281.0	280.8
		% SRC	100.0	67.4	100.0

XPS results show that in the Ru/C sample, the Ru^{4+} species are likely coordinated by carbon ligands belonging to the support (e.g. COO^-), finally hampering the reduction of most of Ru^{4+} species. Moreover, after 5 cycles of reaction, the progressive oxidation of both the carbon support and ruthenium in Ru/C_ 5c leads to catalyst deactivation. Interestingly, XPS results are in agreement with the fact that the diffraction fringes observed by HR-TEM, ascribed to metallic Ru in the Ru/C catalyst, were not detected with Ru/C_ 5c.

With the $(RuO_2)_{0.038}\cdot(SiO_2)_{0.962}$ sample (XP spectra not shown) only oxidized Ru^{x+} species were detected, mainly corresponding to Ru^{4+} species, but also to a limited fraction of Ru^{3+} species (*ca.* 1.0 %). Though it must be considered that the curve-fit of the Ru(3d5/2) line was complicated by the occurrence of the Ru^{4+} satellite peak at nearly the same binding energy of Ru^{3+} (282.5 eV), TPR analysis (Figure S1) showed at reduction peak at 130 °C ascribed to reduction of Ru^{3+} from the salt used as precursor. This was also confirmed by the presence of a peak at 529.4 eV in the O 1s region, ascribable to the presence of RuO_2, in agreement with TPR analysis (*vide supra*) and Raman spectroscopy (*vide infra*). Upon reduction, the Ru^{4+} component remarkably decreased (Figure 8) and, correspondingly, an overall 78 % of reduced ruthenium species was determined with the Ru-SiO_2 catalyst. Accordingly, in the O 1s region the RuO_2-related component decreased as well.

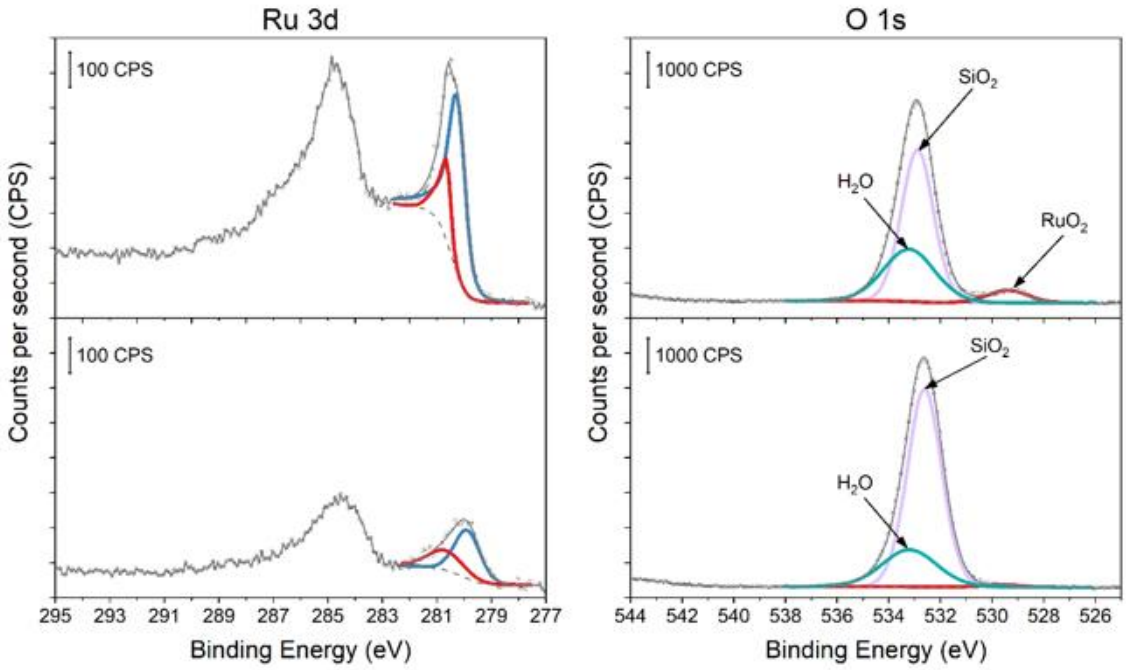

Figure 8. XP spectra of the Ru(3d5/2) core level, along with the O(1s) core levels of Ru-SiO_2 (topo panel) and Ru- SiO_2_5c (bottom panel).

As reported in Table 4, the position of the line assigned to reduced Ru species is found at higher BE values with respect to literature values[28]: this result, as reported by Carrillo *et al.*[29] for a similar system, can be likely ascribed to the formation of (at least partially) reduced ruthenium species in a zero-oxidation state, that are stabilized by a strong interaction with the SiO_2 support. With the Ru-SiO_2_5c catalyst, the line of the Ru^0 species was found at 279.7 eV, *i.e.* a value which is very close to the reference for metallic Ru indicating the complete reduction of 64 % ruthenium during the reaction, as a result of the catalyst self-activation, likely due to Ru capability to create active sites for hydrogen splitting, as also measured by TPR showing H_2 consumption above 500 °C (Figure S1). Accordingly, in the O 1s region the line due to RuO_2 was nearly absent (*ca.* 1.0 %, Table 4).

Raman spectroscopy, a valuable tool to identify different oxidation states Ru (with the exception of metallic ruthenium),[16,30,31] may efficiently detect crystalline RuO_2, though amorphous ruthenium oxide does not exhibit Raman peaks in the wavelength region investigated in this study[32]: with the $(RuO_2)_{0.038}\cdot(SiO_2)_{0.962}$ powder (trace a in Figure 9A) three signals at about 641, 703, and 520 cm^{-1} are detected, respectively ascribed to the A_{1g}, B_{2g}, and E_g main Raman modes of crystalline RuO_2.[27] Conversely, with both Ru-SiO_2 and Ru_SiO_2_5c

(traces b and c in Figure 9A), no Raman bands related to crystalline RuO_2 are detected, in agreement with a catalyst reduction and previously reported characterization.

Table 4. Values of binding energy (BE, eV) and surface relative concentration (SRC, %) as obtained by the curve-fitting procedure carried out on the XP analyses of $(RuO_2)_{0.038}\cdot(SiO_2)_{0.962}$, Ru-$SiO_2$ and Ru/SiO_2_5c catalysts.

	Sample		**$(RuO_2)_{0.038}\cdot(SiO_2)_{0.962}$**	**Ru-SiO_2**	**Ru-SiO_2_5c**
O 1s	RuO_2	BE [eV]	529.4	529.4	529.6
		%SRC	11.4	6.4	1.0
	SiO_2	BE [eV]	533.2	532.9	532.6
		%SRC	38.3	60.2	76.1
	H_2O	BE [eV]	533.2	533.2	533.2
		%SRC	50.3	33.4	22.9
Ru $3d_{5/2}$	Ru	BE [eV]	-	280.2	279.7
		%SRC	-	79.0	69.4
	Ru^{4+}	BE [eV]	280.6	280.6	280.3
		%SRC	99.0 (*ca.* 1.0 Ru^{3+})	21.0	30.6

Only a broad band at about 490 cm^{-1} is clearly seen in the Ru-SiO_2_5c. In this frequency range the symmetric stretching of Si-O-Si bridges are active. Usually, for fused silica glass the bands occurring at 495 cm^{-1} (D_1 defect band) and 605 cm^{-1} (D_2 defect band) were assigned to symmetric stretching modes of Si-O-Si bridges in regular fourfold rings and strained threefold rings of SiO_4 tetrahedra, respectively.[33,34] For gel-derived glasses the position and the relative intensities of these bands are very sensitive to the heat-treatments required to transform the wet gel into the corresponding glass, and the shift at 490 cm^{-1} of the D_1 band was elsewhere assigned to symmetric stretch vibrations of three oxygen atoms symmetrically bonded to a terminal silanol group: O_3SiOH.[35,36] The D_1/D_2 relative intensities ratio was related to the amount of chemisorbed water in the siloxane network of silica aerogels.[37] The siloxane bridges belonging to strained $(SiO)_3$-rings will be attacked more easily by water producing three O_3SiOH tetrahedra and, at the same time, increasing the D_1/D_2 ratio. Actually, the progressive self-activation observed for Ru-SiO_2 catalysts can be related to gradual water chemisorption occurring in each reaction cycle. Both Ru-SiO_2 and Ru-SiO_2_5c

XPS analyses showed the presence of Ru and Ru^{4+} species while TEM characterization evidenced a different distribution of Ru nanoparticles size in these samples. The Ru dispersion calculated from CO chemisorption experiments by assuming a Ru/CO stoichiometry equal to 1:1, was indeed equal to 8.66 % for Ru/SiO_2 and 88.80 % for Ru-C. The poor Ru dispersion in $Ru\text{-}SiO_2$ is also in agreement with its self-activating behaviour. The high Ru dispersion in the Ru-C catalyst confirms its very fast activation.

The water chemisorption gradually produces non-bridging oxygen species, whose charge will be balanced by Ru^{4+} and, in turn, high dispersion into the siloxane network of these species is favored. Accordingly, an increase of the BET surface area was measured with the $Ru\text{-}SiO_2$_5c sample, likely due to the opening of $(SiO)_3$-rings. The reaction environment reduces the Ru^{4+} species to metallic ruthenium, ultimately leading to the thin crystalline layers seen in Figure 6. This process partially counteracts the spontaneous oxidation of Ru nanoparticles avoiding the catalyst deactivation. Regarding the carbon-supported catalysts, both Ru/C and Ru/C_5c (i.e. traces a and b in Figure 9A) exhibit only the amorphous carbon Raman bands, with typical D (around 1354 cm^{-1}) and G (around 1601 cm^{-1}) bands.[38] It is worth noting that literature reports the co-existence of RuO_2 crystals with both porous carbon,[39] graphite[40] and carbon nanotubes.[41] Thus, the absence of RuO_2-crystal related Raman bands suggest the presence of metallic Ru, and/or amorphous RuO_2, in agreement with HR-TEM and XPS findings. No sorbitol was detected on both samples (sorbitol reference is reported in trace c of Figure 9B).

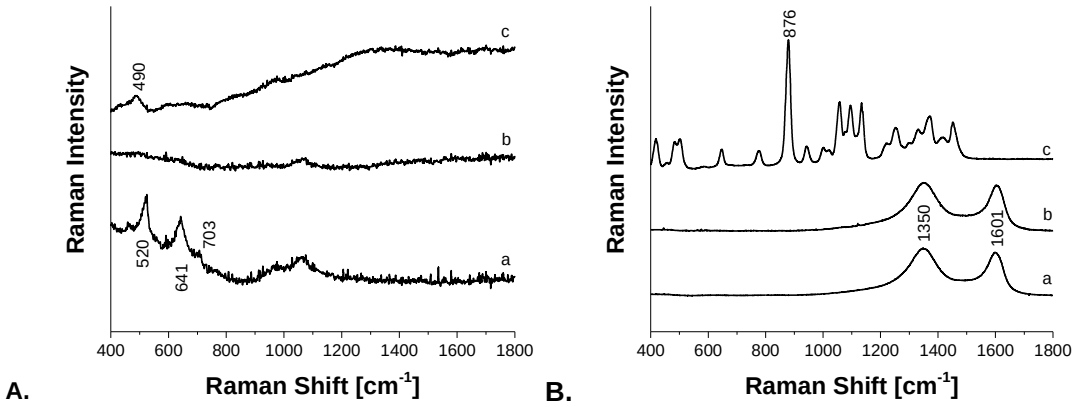

Figure 9. Raman spectra collected on: A. $(RuO_2)_{0.038}\cdot(SiO_2)_{0.962}$ (a), $Ru\text{-}SiO_2$ (b), $Ru\text{-}SiO_2$_5c (c). B. Ru/C (a), Ru/C_5c (b), sorbitol (c). Excitation line 514 nm, 4 mW at the sample.

4 Conclusions

A new $(RuO_2)_{0.038}\cdot(SiO_2)_{0.962}$ nanomaterial was synthesized by one-pot sol-gel route. The catalytic performance of the developed catalyst was investigated in the glucose hydrogenation

reaction, in aqueous phase and mild conditions and compared with commercial Ru/C catalyst. The TOF values clearly show that the Ru/C activity is already lost in 5 h of reaction, whereas Ru-SiO_2 is getting activated in the first 5 h. In Ru/C catalyst the highly dispersed small Ru NPs promotes a high activity only during the first cycle. The rapid deactivation that was observed is mostly related to morphological changes of Ru nanoparticles, not efficiently stabilized by the C support, associated to a progressive oxidation of both the carbon support and ruthenium.

On the contrary, with the Ru-SiO_2 catalyst, initially characterized by a heterogeneous distribution of the Ru active phase, smaller Ru nanoparticles are fairly stabilized by the interaction with the SiO_2 support, likely because of the adopted synthesis procedure. In addition, water chemisorption, occurring during reaction cycles, produces a modification in the siloxane surface bridges, favoring a fair dispersion of ruthenium species. Further reduction of these species in the reaction environment was observed due to the synergic effect of both H_2 and glucose witch actually act as *in situ* reducing agents for the Ru/SiO_2. that ultimately proved to be a self-activating catalyst.

Acknowledgments

List of symbols

$c_{Glucose}$	Glucose concentration, [mol/L]
d_i	Diameter of particle *i*, [nm]
d_m	Mean particle diameter, [nm]
n	Moles, [mol]
n_i	Number of particles *i* with d_i diameter, [-]
p	Pressure, [MPa]
r_i	Mean radius of the size class containing n_i particles, [nm]
SSA	Specific surface area, [m^2/g]
SA	Surface area, [m^2]
t	Time, [min]
T	Temperature, [°C]
TOF	Turnover frequency, [s^{-1}]
T_R	Reduction temperature, [°C]
$X_{glucose}$	Glucose conversion, [-]

Greek symbols

$\Phi_{sorbitol}$	Sorbitol selectivity, [-]
ρ_{Ru}	Volumetric mass of Ru, [g/cm^3]

References

(1) Huber, G.W.; Iborra, S.; Corma, A. Synthesis of transportation fuels from biomass: chemistry, catalysts, and engineering. *Chem. Rev.* **2006**, *106*, 4044-4098.

(2) Kusserow, B.; Schimpf, S.; Claus, P. Hydrogenation of Glucose to Sorbitol over Nickel and Ruthenium Catalysts. *Adv. Synth. Catal.* **2003**, *345*, 289-299.

(3) Aho, A.; Roggan, S.; Simakova, O.A.; Salmi, T.; Murzin, D.Y. Structure sensitivity in catalytic hydrogenation of glucose over ruthenium. *Catal. Today* **2015**, *241*, 195-199.

(4) Schiweck, H.; Bar, A.; Vogel, R.; Schwarz, E.; Kunz, M. Ullmann's Encyclopedia of Industrial Chemistry, Wiley, Weinheim, 1999.

(5) van Gorp, K.; Boerman, E.; Cavenaghi, C.V.; Berben, P.H. Catalytic hydrogenation of fine chemicals: sorbitol production. *Catal. Today* **1999**, *52*, 349-361.

(6) Wisniak, J.; Simon, R. Hydrogenation of Glucose, Fructose, and Their Mixtures. *Ind. Eng. Chem. Prod. Res. Dev.* **1979**, *18*, 50-57.

(7) Hoffer, B.W.; Crezee, E.; Mooijiman, P.R.M.; van Langeveld, A.D.; Kapteijin, F.; Moulijn, J.A. Carbon supported Ru catalysts as promising alternative for Raney-type Ni in the selective hydrogenation of D-glucose. *Catal. Today* **2003**, *79*, 35-41.

(8) Russo, V.; Kilpio, T.; Di Serio, M.; Tesser, R.; Santacesaria, E.; Murzin, D. Y.; Salmi, T. Dynamic non-isothermal trickle bed reactor with both internal diffusion and heat conduction: arabinose hydrogenation as a case study. *Chem. Eng. Res. Des.* **2015**, *102*, 171-185.

[9] Besson, M.; Gallezot, P. Deactivation of metal catalysts in liquid phase organic reaction. *Catal. Today* **2003**, *81*, 547-559.

(10) Arena, B.J. Deactivation of ruthenium catalysts in continuous glucose hydrogenation. *Appl. Catal.* **1992**, *87*, 219-229.

(11) Zhang, J.; Lin, L.; Zhang, J.; Shi, J. Efficient conversion of D-glucose into D-sorbitol over MCM-41 catalyst prepared by a formaldehyde reduction process. *Carbohydr. Res*. **2011**, *346*, 1327-1332.

(12) Romero, A.; Nieto-Márquez, A.; Alonso, E. Bimetallic Ru:Ni/MCM-48 catalysts for the effective hydrogenation of D-glucose into sorbitol. *Appl. Catal. A-Gen.* **2017**, *529*, 49-59.

(13) Mishra, D.K.; Lee, J.M.; Chang, J.S.; Hwang, J.S. Liquid phase hydrogenation of D-glucose to D-sorbitol over the catalyst (Ru/Ni-TiO_2) of ruthenium on NiO-modified TiO_2 support. *Catal. Today* **2012**, *185*, 104-108.

(14) Yadav, M.; Mishra, D.K.; Hwang, J.S. Catalytic hydrogenation of xylose to xylitol using ruthenium catalyst on NiO modified TiO_2 support. *Appl. Catal.* **2012**, *425*, 110-116.

(15) Mishra, D.K.; Dabbawala, A.A.; Park, J.J.; Jhung, S.H.; Hwang, J.S. Selective hydrogenation of D-glucose to D-sorbitol over HY zeolite supported ruthenium nanoparticles catalysts. *Catal. Today* **2013**, *232*, 99-107.

(16) Mishra, D.K.; Dabbawala, A.A.; Hwang J.S. Ruthenium nanoparticles supported on zeolite Y as an efficient catalyst for selective hydrogenation of xylose to xylitol. *J. Mol. Catal. A-Chem.* **2013**, *376*, 63-70.

(17) Minieri, L.; Esposito, S.; Russo, V.; Bonelli, B.; Di Serio, M.; Silvestri, B.; Vergara, A.; Aronne. A. A New Sol-Gel Ru-Nb-Si Mixed-Oxides Bifunctional Catalyst for the Hydrogenation of Levulinic Acid in Aqueous Phase. *Chem. Cat. Chem.* **2017**, *9*, 1-12.

(18) Luciani, G.; Costantini, A.; Silvestri, B.; Tescione, F.; Branda, F.; Pezzella, A. Synthesis, structure and bioactivity of pHEMA/SiO_2 hybrids derived through in situ sol–gel process. *J. Sol-Gel Sci. Technol.* **2008**, *46*, 166-175.

(19) Silvestri, B.; Pezzella, A.; Luciani, G.; Costantini, A.; Tescione, F.; Branda, F. Heparin conjugated silica nanoparticle synthesis. *Mat. Sci. Eng. C* **2012**, *32*, 2037-2041.

(20) Tristany, M.; Philippot, K.; Guari, Y., Collière; V., Lecante, P.; Chaudret, B. Synthesis of composite ruthenium-containing silica nanomaterials from amine-stabilized ruthenium nanoparticles as elemental bricks. *J. Mat. Chem.* **2010**, *20*, 9523-9530.

(21) Silvestri, B.; Guarnieri, D.; Luciani, G.; Costantini, A.; Netti, P. A.; Branda, F. Fluorescent (rhodamine), folate decorated and doxorubicin charged, PEGylated nanoparticles synthesis. *J. Mater. Sci. Mater. M.* **2012**, *23*, 1697-1704.

(22) García-García, R.F.; Fernández-García, M.; Newton, M.A.; Rodríguez-Ramos, I.; Guerrero-Ruiz, A. Following the Evolution of Ru/Activated Carbon Catalysts during the Decomposition–Reduction of the Ru(NO)(NO_3)$_3$ Precursor. *Chem. Cat. Chem.* **2013**, *5*, 2446-2452.

(23) Peng, G.; Gramm, F.; Ludwigac, C.; Vogel, F. Effect of carbon surface functional groups on the synthesis of Ru/C catalysts for supercritical water gasification. *Catal. Sci. Technol.* **2015**, *5*, 3658–3666.

(24) Esposito, S.; Dell'Agli, G.; Marocco, A.; Bonelli, B.; Allia, P.; Tiberto, P.; Barrera, G.; Manzoli, M.; Arletti, R.; Pansini, M. Magnetic metal-ceramic nanocomposites obtained from cation-exchanged zeolite by heat treatment in reducing atmosphere. *Micropor. Mesopor. Mat.* **2018**, *268*, 131-143.

(25) Dmitriev, R. V.; Zubareva, N. D.; Vedenyapin, A. A.; Klabunovskii, E. I.; Minachev, K.M. Chemisorption and hydrogen spillover on framework ruthenium catalysts. *B Acad Sci USSR Ch+* **1988**, *37*, 1523-1526.

(26) Mazzier, V.; Figoli, N.; Pascual, F.-C.; L'Argentiére, P. Effect of the support on the selective hydrogenation of benzeneover ruthenium catalysts. 1. Al_2O_3 and SiO_2 *Catal. Lett.* **2005**, *102*, 79-82.

(27) Gatti, M.N.; Lombardi, B.; Gazzoli, D.; Santori, G.F.; Pompeo, F.; Nichio, N.N. Hydrothermal Stability of Ru/SiO_2–C: A Promising Catalyst for Biomass Processing through Liquid-Phase Reactions. *Catalysts* **2017**, *7*, 6.

(28) Morgan, D.J. Resolving ruthenium: XPS studies of common ruthenium materials. *Surf. Interface Anal*. **2015**, *47*, 1072-1079.

(29) Carrillo, A.I.; Schmidt, L.C.; Marín, M.L.; Scaiano, J.C. Mild synthesis of mesoporous silica supported ruthenium nanoparticles as heterogeneous catalysts in oxidative Wittig coupling reactions. *Cat. Sci. Technol.* **2014**, *4*, 435-440.

(30) Vergara, A.; D'Errico, G.; Montesarchio, D.; Mangiapia, G.; Paduano, L.; Merlino, A. Interaction of anticancer Ruthenium compounds with proteins: High resolution X-ray structures and Raman microscopy studies of the adduct between hen egg white lysozyme and AziRu. *Inorg. Chem.* **2013**, *52*, 4157-4159.

(31) Vergara, A.; Russo Krauss, I.; Montesarchio, D.; Paduano, L.; Merlino, A. Investigating the ruthenium metallation of proteins: X-ray structure and Raman microspectroscopy of the complex between RNase A and AziRu. *Inorg. Chem.* **2013**, *52*, 10714-10716.

(32) Tsuji, E.; Imanishia, A.; Fukui, K.I.; Nakato, Y. Electrocatalytic activity of amorphous RuO_2 electrode for oxygen evolution in an aqueous solution. *Electrochim. Acta* **2011**, *56*, 2009-2016.

(33) Galeener F. L.; Luckovsky, G. Longitudinal Optical Vibrations in Glasses: GeO_2 and SiO_2. *Phys. Rev. Lett.* **1976**, *37*, 1474.

(34) Galeener, F. L. Band limits and the vibrational spectra of tetrahedral glasses. *Phys. Rev. B* 1979, 19, 4292.

(35) Mulder, C. A. M.; Damen, A. A. J. M. The origin of the "defect" 490 cm^{-1} Raman peak in silica gel. *J. Non-Cryst. Solids* **1987**, *93*, 387-394.

(36) Humbert B. Estimation of hydroxyl density at the surface of pyrogenic silicas by complementary NMR and Raman experiments. *J. Non-Cryst. Solids* **1995**, *191*, 29-37.

(37) Riegel, B.; Hartmann, I.; Kiefer, W.; Grob, J.; Fricke, J. Raman spectroscopy on silica aerogels. *J. Non-Cryst. Solids* **1997**, *211*, 294-298.

(38) Alfè, M.; Gargiulo, V.; Di Capua, R.; Chiarella, F.; Rouzaud, J.N.; Vergara, A; Ciajolo, A. Wet Chemical Method for Making Graphene-like Films from Carbon Black. *ACS Appl. Mater. Inter.* **2012**, *4*, 4491-4498.

(39) Pico, F.; Morales, E.; Fernandez, J.A.; Centeno, T.A.; Ibanez, J.; Rojas, R.M.; Amarilla, J.M.; Rojo, J.M. Ruthenium oxide/carbon composites with microporous or mesoporous carbon as support and prepared by two procedures. A comparative study as supercapacitor electrodes. *Electrochim. Acta* **2009**, *54*, 2239-2245.

(40) Wang, N.; Li, D.; Yu, L.; Yu, X.; Sun, T. Preparation of RuO_2/Nano-Graphite Cathode for Electrocatalytic Degradation of Phenol. *Int. J. Electrochem. Sci.* **2015**, *10*, 9824-9836.

(41) Kim, J.Y.; Kim, K.H.; Park, S.H.; Kim, K.B. Microwave-polyol synthesis of nanocrystalline ruthenium oxide nanoparticles on carbon nanotubes for electrochemical capacitors. *Electrochim. Acta* **2010**, *55*, 8056-8061.

SYNOPSIS

S. Esposito, B. Silvestri, V. Russo, B. Bonelli, M. Manzoli, F.A. Deorsola, A. Vergara, A. Aronne, M. Di Serio